

# Exploring the High-Temperature Electrical Performance of $\text{Ca}_{3-x}\text{La}_x\text{Co}_4\text{O}_9$ Thermoelectric Ceramics for Moderate and Low Substitution Levels

Gabriel Constantinescu <sup>1,\*</sup>, Shahed Rasekh <sup>1</sup>, Parisa Amirkhizi <sup>1</sup>, Daniela V. Lopes <sup>1</sup>, Miguel A. Vieira <sup>1</sup>, Andrei V. Kovalevsky <sup>1</sup>, Juan C. Diez <sup>2</sup>, Andres Sotelo <sup>2</sup>, Maria A. Madre <sup>2</sup> and Miguel A. Torres <sup>2</sup>

<sup>1</sup> Department of Materials and Ceramics Engineering, CICECO—Aveiro Institute of Materials, University of Aveiro, 3810-193 Aveiro, Portugal; shahedvrm@ua.pt (S.R.); parisa.amirkhizi@ua.pt (P.A.); daniela.rosendo.lopes@ua.pt (D.V.L.); miguelamado@ua.pt (M.A.V.); akavaleuski@ua.pt (A.V.K.)

<sup>2</sup> Instituto de Nanociencia y Materiales de Aragón (INMA), CSIC-Universidad de Zaragoza, 50009 Zaragoza, Spain; monux@unizar.es (J.C.D.); asotelo@unizar.es (A.S.); amadre@unizar.es (M.A.M.); matorres@unizar.es (M.A.T.)

\* Correspondence: gabriel.constantinescu@ua.pt

**Citation:** Constantinescu, G.; Rasekh, S.; Amirkhizi, P.; Lopes, D.V.; Vieira, M.A.; Kovalevsky, A.V.; Diez, J.C.; Sotelo, A.; Madre, M.A.; Torres, M.A.; et al. Exploring the High-Temperature Electrical Performance of  $\text{Ca}_{3-x}\text{La}_x\text{Co}_4\text{O}_9$  Thermoelectric Ceramics for Moderate and Low Substitution Levels. *Symmetry* **2021**, *13*, 782. <https://doi.org/10.3390/sym13050782>

Academic Editor: José Carlos R. Alcantud

Received: 19 March 2021

Accepted: 29 April 2021

Published: 1 May 2021

**Publisher's Note:** MDPI stays neutral with regard to jurisdictional claims in published maps and institutional affiliations.



**Copyright:** © 2021 by the authors. Licensee MDPI, Basel, Switzerland. This article is an open access article distributed under the terms and conditions of the Creative Commons Attribution (CC BY) license (<http://creativecommons.org/licenses/by/4.0/>).

**Abstract:** Aliovalent substitutions in  $\text{Ca}_3\text{Co}_4\text{O}_9$  often result in complex effects on the electrical properties and the solubility, and impact of the substituting cation also depends largely on the preparation and processing method. It is also well-known that the monoclinic symmetry of this material's composite crystal structure allows for a significant hole transfer from the rock salt-type  $\text{Ca}_2\text{CoO}_3$  buffer layers to the hexagonal  $\text{CoO}_2$  ones, increasing the concentration of holes and breaking the electron–hole symmetry from the latter layers. This work explored the relevant effects of relatively low La-for-Ca substitutions, for samples prepared and processed through a conventional ceramic route, chosen for its simplicity. The obtained results show that the actual substitution level does not exceed 0.03 ( $x < 0.03$ ) in  $\text{Ca}_{3-x}\text{La}_x\text{Co}_4\text{O}_9$  samples with  $x = 0.01, 0.03, 0.05$  and  $0.07$  and that further introduction of lanthanum results in simultaneous  $\text{Ca}_3\text{Co}_4\text{O}_9$  phase decomposition and secondary  $\text{Ca}_3\text{Co}_2\text{O}_6$  and  $(\text{La},\text{Ca})\text{CoO}_3$  phase formation. The microstructural effects promoted by this phase evolution have a moderate influence on the electronic transport. The electrical measurements and determined average oxidation state of cobalt at room temperature suggest that the present La substitutions might only have a minor effect on the concentration of charge carriers and/or their mobility. The electrical resistivity values of the  $\text{Ca}_{3-x}\text{La}_x\text{Co}_4\text{O}_9$  samples with  $x = 0.01, 0.03$  and  $0.05$  were found to be ~1.3 times (or 24%) lower (considering mean values) than those measured for the pristine  $\text{Ca}_3\text{Co}_4\text{O}_9$  samples, while the changes in Seebeck coefficient values were only moderate. The highest power factor value calculated for  $\text{Ca}_{2.99}\text{La}_{0.01}\text{Co}_4\text{O}_9$  (~0.28 mW/K<sup>2</sup>m at 800 °C) is among the best found in the literature for similar materials. The obtained results suggest that low rare-earth substitutions in the rock salt-type layers can be a promising pathway in designing and improving these p-type thermoelectric oxides, provided by the strong interplay between the mobility of charge carriers and their concentration, capable of breaking the electron–hole symmetry from the conductive layers.

**Keywords:** thermoelectric calcium cobaltite; rock salt-type layers; rare-earth substitutions; ceramic route; electrical performance

## 1. Introduction

Thermoelectric (TE) materials have the ability to directly transform temperature gradients into electrical power, thanks to the Seebeck effect. The efficiency of this conversion is normally quantified using the dimensionless figure of merit ZT, equal to  $S^2T/\rho\kappa$  (in which  $S^2/\rho$  is also called the power factor, PF, representing the electrical performance),

where  $S$ ,  $\rho$ ,  $\kappa$  and  $T$  are the Seebeck coefficient (or thermopower), electrical resistivity, total thermal conductivity and absolute temperature, respectively [1]. The focus on TE materials capable of direct solid-state energy conversion using high-temperature waste heat is increasingly rising due to some environmental challenges imposed by global warming effects [2–4]. These renewable energy materials can be used in various high-temperature power generation applications, such as waste heat recovery devices [5] and solar TE generators [6]. They can also be used in heating/refrigeration devices [7], owing to the inverse Peltier effect.

Considering the expression for ZT, high-performance TE materials must simultaneously possess large Seebeck coefficients and low electrical resistivity and thermal conductivity values. Large temperature gradients also result in a higher TE conversion efficiency. Generally, a low electrical resistivity is also necessary to minimize the Joule heating effect, while a low thermal conductivity can lead to different temperature gradients being maintained between the involved hot and cold sides.

Modern commercial TE modules/devices constructed from intermetallic compounds such as  $\text{Bi}_2\text{Te}_3$  [8] or  $\text{CoSb}_3$  [9], with ZT values around one, are industrially used in some niche applications (such as remote probing/sensing) at relatively low temperatures. These materials are incapable of working at high temperatures in air because of the degradation and/or evaporation of the heavy constitutive elements, which are also expensive, scarce and/or toxic and can pose a real threat to the environment and human health. The stability and working temperature limitations, characteristic for “classical” TE materials, were left behind with the discovery of promising TE properties in  $\text{NaCo}_2\text{O}_4$  ceramics [10] in 1997. From this point onwards, substantial work has been performed on other cobaltite species with promising TE performance, especially at high temperatures and in oxygen-rich environments. The *p*-type Bi-AE-Co-O-based (AE: alkaline earth metals) materials [11–13] and the so-called  $\text{Ca}_3\text{Co}_4\text{O}_9$  compound [14,15] are regarded as the most promising candidates from this particular class of functional electroceramics.

Crystallographic studies of these layered cobaltites have revealed an intrinsically nanostructured nature. These materials possess a complex monoclinic crystal structure (unit cell), made from two distinct layers, alternatively stacked in the direction of the *c*-axis, having all the crystal parameters equal, except the *b*-axis lengths [16,17]. A triple distorted rock salt (RS)-type  $[\text{Ca}_2\text{CoO}_3]$  insulating layer (regarded as the first subsystem) is sandwiched between two hexagonal CdI<sub>2</sub>-type  $[\text{CoO}_2]$  common conductive layers (regarded as the second subsystem), and a “misfit” or incommensurability ratio results from the two different *b*-axis lengths. These layered structures exhibit high electrical conductivity and low thermal conductivity, resulting in figures of merit comparable to those of traditional intermetallic TEs, while exhibiting superior thermal and chemical stability, especially at higher temperatures.

The incommensurability ratio and/or the electrical charge from the RS-type layers situated between the  $[\text{CoO}_2]$  ones have been found to govern the Seebeck coefficient values from these materials [16]. It was also reported that the two distinct Co sites from  $\text{Ca}_3\text{Co}_4\text{O}_9$  play two completely different roles in its TE behavior, which are to provide charge carriers to the  $\text{CoO}_2$  layers and to conduct holes along the  $\text{CoO}_2$  layers [18]. This has allowed the TE properties of this class of compounds to be tailored via chemical substitutions, such as  $\text{Sb}^{3+}$  for  $\text{Ca}^{2+}$  in  $\text{Ca}_3\text{Co}_4\text{O}_9$  [19] or  $\text{Pb}^{2+}$  for  $\text{Bi}^{3+}$  in  $\text{Bi}_2\text{Sr}_2\text{Co}_{1.8}\text{O}_x$  [20] or  $\text{Bi}_2\text{Ca}_2\text{Co}_{1.7}\text{O}_x$  [21]. Other significant improvements in the TE properties of these materials can be achieved by additions of metallic Ag, where an increase in the material’s electrical performance is produced by improving the electrical contacts between the grains [22–25].

The high crystallographic/structural anisotropy from these materials leads to the formation of plate-like grains during sintering processes, which opens the possibility to preferentially align them using different methods that take advantage of their intrinsic properties. Such processing/texturing processes performed on bulk, polycrystalline materials would allow for the alignment of the conducting *ab* planes, which in turn would lead to electrical properties comparable to those obtained in single crystals. Various methods

have been reported to be successful in producing well-aligned materials with high density and improved electrical properties in these cobaltites or in similar anisotropic ceramic systems, such as uniaxial hot-pressing (HP) [26], spark plasma sintering (SPS) [27], microwave sintering (MS) [28], (electrically assisted) laser floating zone melting ((EA)LFZ) [29,30] and reactive templated grain growth (TGG) [31]. These techniques have the main advantage of producing dense materials with very low electrical resistivity values, owing to the preferential alignment of the conducting planes with the direction of current flow. Unfortunately, they possess some important drawbacks, such as the high prices associated with the spark plasma sintering systems/processes and the relatively long processing times involved in the uniaxial hot-pressing and the reactive templated grain growth methods.

The calcium substitution with lanthanum in  $\text{Ca}_3\text{Co}_4\text{O}_9$  materials has been studied in several works aimed at TE [32,33] and solid oxide fuel cell (SOFC) [34] applications. Good prospects for tailoring TE performance were demonstrated for the materials prepared by wet chemistry methods and for those consolidated using SPS. The implemented substitution levels were remarkably large (up to  $x = 0.3$  in  $\text{Ca}_{3-x}\text{La}_x\text{Co}_4\text{O}_9$ ), while little or no attention was given to low and moderate values of  $x$ . The attained substitution level is also significantly affected by the preparation/processing route. This work explores the relevant effects of relatively low substitutions of La for Ca on the microstructure and high-temperature electrical properties of  $\text{Ca}_{3-x}\text{La}_x\text{Co}_4\text{O}_9$  ( $x = 0.00, 0.01, 0.03, 0.05$  and  $0.07$ ) ceramics, prepared through a classical solid-state (ceramic) route. This conventional synthetic method was chosen for its simplicity, reduced pollution, low costs, industrial importance and scalability, despite its known major disadvantage of producing low surface area products that can possibly exhibit low reactivity in the sintering stage. The electron–hole symmetry from the conductive  $\text{CoO}_2$  layers was expected to change as a result of a mobile hole concentration and/or mobility increase, produced by the incorporation of the trivalent lanthanum ions into the RS-type sublattices, to a certain extent. The compositional and morpho-structural modifications produced by the partial substitutions are related to the changes in TE performance.

## 2. Materials and Methods

$\text{Ca}_{3-x}\text{La}_x\text{Co}_4\text{O}_9$  bulk polycrystalline ceramics, with  $x = 0.00, 0.01, 0.03, 0.05$  and  $0.07$ , were prepared through a conventional solid-state synthesis route using stoichiometric amounts of  $\text{CaCO}_3$  (Sigma-Aldrich ((Darmstadt, Germany)),  $\geq 99\%$ ),  $\text{La}_2\text{O}_3$  (Sigma-Aldrich,  $\geq 99.9\%$ ) and  $\text{CoO}$  (Panreac (Barcelona, Spain),  $99.5\%$ ) commercial powders as precursors. Appropriate quantities of starting powders were carefully mixed and ball-milled for 30 min at 8 relative centrifugal force (RCF) in acetone using an agate ball mill. The resulting ceramic slurries were dried until full evaporation of the acetone. The dry mixtures were then manually ground in an agate mortar for a final homogenization, followed by 2 annealing cycles performed in air, at  $750$  and  $800$  °C for 12 h each, with an intermediate manual grinding in order to assure the complete decomposition of any remaining carbonates [35] and improve the reactivity of the ceramic powders in the following sintering stage. After the two thermal treatments, rectangular, bar-shaped samples ( $3 \times 2.5 \times 14$  mm<sup>3</sup>) were obtained by uniaxial pressing (400 MPa, one minute) of appropriate amounts of corresponding green powders. The consolidated green bars were subsequently sintered in air, at  $910$  °C for 24 h, with a final, free cooling [35].

X-ray diffraction (XRD) analyses (at room temperature, with  $2\theta$  angles between  $5$  and  $70$  degrees and a step of  $0.03$  ° $2\theta$ ) were performed on powdered, sintered samples to identify the phase composition in each case, using Rigaku D/max-B powder XRD equipment working with  $\text{CuK}\alpha$  radiation ( $\lambda = 1.54$  Å). The corresponding lattice parameters (including  $\beta$  angles and unit cell volumes) were calculated using a profile matching method through Rietveld refinement, with the FullProf program [36].

Morphological and microstructural studies were performed on longitudinal polished surfaces of selected samples from each composition, with the help of a field emission scanning electron microscope (FESEM, Carl Zeiss Merlin) equipped with an energy dispersive spectrometry (EDS) analyzer. Several micrographs (taken using both backscattered and secondary electrons, using an acceleration voltage of 20 kV) from each composition were taken to analyze the different phases present and their distribution in the bulk materials.

Apparent density calculations (using the samples' masses and volumes) were performed for several sintered samples from each composition (to minimize measurement errors) using the theoretical density value of 4.677 g/cm<sup>3</sup> for the Ca<sub>3</sub>Co<sub>4</sub>O<sub>9</sub> phase [37].

The oxygen content from all compositions was determined through room-temperature cerimetry in order to calculate the mean cobalt valence (Co<sup>3+</sup> + Co<sup>4+</sup>) from the conductive layers using a procedure described in previous works [38].

The electrical resistivity ( $\rho$ ) and Seebeck coefficient ( $S$ ) values were simultaneously measured using the standard four-point probe DC technique in a commercial LSR-3 measurement system (Linseis, GmbH (Selb, Germany)) in a steady-state mode and at temperatures ( $T$ ) between 50 and 800 °C, under inert He atmosphere. The estimated experimental error of the measured electrical resistivity and Seebeck coefficient values did not exceed 3–5% and 5–7%, respectively.

From the measured resistivity values, the activation energies (from the semiconducting regime) for each composition were calculated and compared with the reference, undoped samples, based on the relationship  $\sigma T \propto \exp(-E_a/k_B T)$ , where  $\sigma$ ,  $T$ ,  $E_a$  and  $k_B$  are the electrical conductivity, absolute temperature, activation energy and Boltzmann constant, respectively. The activation energies were obtained from the  $\ln(\sigma T)$  vs.  $1000/T$  plots, from the fitting slopes below  $T^*$ , which represents the semiconducting-to-metallic transition temperature and which is clearly marked in all the corresponding modified Arrhenius plots. The fitting slopes from the metallic conductivity regime are also shown in these plots (linear fits are just visual guides) to clearly indicate  $T^*$ .

The PF values were calculated from the determined electrical resistivity and Seebeck coefficient values (using the  $S^2/\rho$  formula, mentioned earlier) and compared with the relevant results from the literature.

All plots were constructed using the KaleidaGraph (Synergy Software, Reading, PA, USA) software. The profile refinement graph was constructed with the WinPLOTR tool [39] from the FullProf suite (ILL.EU).

### 3. Results and Discussion

The powder XRD patterns of the different Ca<sub>3-x</sub>La<sub>x</sub>Co<sub>4</sub>O<sub>9</sub> samples are displayed in Figure 1, between 5 and 40 degrees for clarity. All samples show very similar diffraction patterns, and the highest peaks (indexed in Figure 1A(a)) in all cases belong to the Ca<sub>3</sub>Co<sub>4</sub>O<sub>9</sub> TE phase, with monoclinic symmetry [37], in agreement with the PDF cards #00-058-0661 [37] and #00-062-0692 and with previously reported results [40–42]. In the same figure, the peak marked with a \* and situated at  $\sim 31^\circ 2\theta$  corresponds to the secondary Ca<sub>3</sub>Co<sub>2</sub>O<sub>6</sub> phase [41,43,44], in agreement with the PDF cards #00-051-0311 [45] and #04-010-0812. Upon the substitution with La, new peaks attributed to the secondary Ca<sub>3</sub>Co<sub>2</sub>O<sub>6</sub> phase start to appear and increase in intensity (Figure 1A(b–e)), proportional to the nominal substitution level. A similar phase evolution was observed previously for Nd-substituted Ca<sub>3</sub>Co<sub>4</sub>O<sub>9</sub> samples [35] for similar substitution levels. However, this tendency is not seen for the Ca<sub>2.93</sub>La<sub>0.07</sub>Co<sub>4</sub>O<sub>9</sub> samples, probably due to the formation of other secondary phases not detected by the XRD technique. When the XRD peaks corresponding to the Ca<sub>3</sub>Co<sub>4</sub>O<sub>9</sub> and Ca<sub>3</sub>Co<sub>2</sub>O<sub>6</sub> phases are analyzed in more detail, a small shift (visible in Figure 1B) to higher  $2\theta$  angles is seen, indicating a slight decrease in the corresponding lattice parameters and unit cell volumes. The corresponding results (and their

standard errors) are presented in Table 1, together with the Rietveld refinement agreement factors, calculated apparent (geometrical) density and activation energy (corresponding to the semiconducting regime of the electrical resistivity) values.

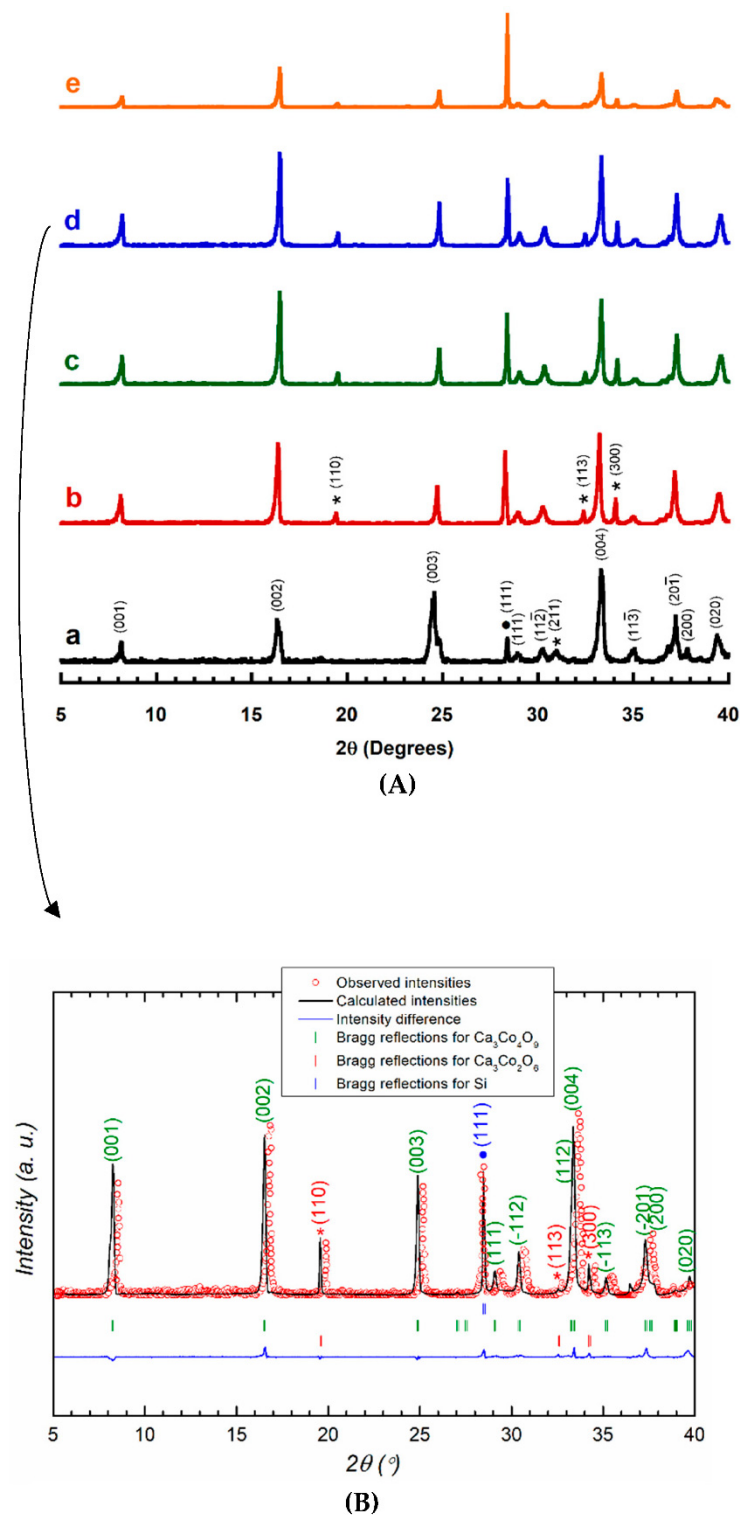


**Figure 1.** (A) Powder XRD patterns obtained for the different  $\text{Ca}_{3-x}\text{La}_x\text{Co}_4\text{O}_9$  samples, with  $x = 0.00$  (a), 0.01 (b), 0.03 (c), 0.05 (d) and 0.07 (e). The peaks from (a) identify the main  $\text{Ca}_3\text{Co}_4\text{O}_9$  phase and those with an asterisk (\*) correspond to the secondary  $\text{Ca}_3\text{Co}_2\text{O}_6$  phase (a and b). The  $\bullet(111)$  plane from (a) belongs to silicon, used as internal reference. (B) Example of a FullProf XRD profile refinement graph (LeBail fitting) for the  $\text{Ca}_{2.95}\text{La}_{0.05}\text{Co}_4\text{O}_9$  samples, showing the crystallographic

planes for the  $\text{Ca}_3\text{Co}_4\text{O}_9$  phase (the other corresponding planes from (A) are also shown, i.e., for Si and for the  $\text{Ca}_3\text{Co}_2\text{O}_6$  phase).

**Table 1.** Lattice parameters ( $a, b, c, \beta, V$ ), agreement factors ( $R_p, R_{wp}$  and  $R_{\text{Bragg}(\text{Ca}_3\text{Co}_4\text{O}_9)}$ ), apparent density ( $\rho_{\text{ap}}$ ) and activation energy ( $E_a$ ) values of the various  $\text{Ca}_{3-x}\text{La}_x\text{Co}_4\text{O}_9$  samples.

x Value in $\text{Ca}_{3-x}\text{La}_x\text{Co}_4\text{O}_9$	a, nm	b, nm	c, nm	$\beta$ , deg	V, nm <sup>3</sup>	$R_p$	$R_{wp}$	$R_{\text{Bragg}(\text{Ca}_3\text{Co}_4\text{O}_9)}$	$\rho_{\text{ap}}$ , g/cm <sup>3</sup>	$E_a$ , meV
0.00	0.4839(3)	0.4563(1)	1.0852(3)	98.10(5)	0.2373(2)	9.22	8.63	7.58	3.39(1)	36.52(7)
0.01	0.4837(3)	0.4548(2)	1.0851(5)	98.12(6)	0.2362(2)	6.42	6.99	5.3	3.35(2)	35.40(1)
0.03	0.4829(2)	0.4543(1)	1.0845(4)	98.13(5)	0.2353(1)	6.78	7.17	4.58	3.33(1)	34.21(3)
0.05	0.4835(2)	0.4546(1)	1.0847(3)	98.14(4)	0.2359(1)	6.02	6.67	4.15	3.36(1)	34.36(7)
0.07	0.4836(2)	0.4561(1)	1.0849(3)	98.14(5)	0.2371(2)	6.24	7.38	4.33	2.55(3)	36.62(1)

The profile matching technique from the Rietveld refinement allowed for the identification of the C12/m1 (base-centered) space group for the  $\text{Ca}_3\text{Co}_4\text{O}_9$  phase in all cases. Furthermore, a supercell approximation was used for the calculation of the lattice parameters of the  $\text{Ca}_3\text{Co}_4\text{O}_9$  phase, for simplicity. The “goodness of fit” is reflected in Figure 1B and the agreement factors from Table 1, where it is easy to see that the best fit was achieved for the 0.05 La-substituted  $\text{Ca}_3\text{Co}_4\text{O}_9$  samples, having the smallest agreement factors from this work. The variation of the unit cell volumes seen in Table 1 is rather minor, being partially provided by the relatively small difference in the ionic radii of  $\text{Ca}^{2+}$  and  $\text{La}^{3+}$  [46] and, presumably, by the low substitution levels attained in the corresponding samples. The calculated unit cell volumes for the  $\text{Ca}_{3-x}\text{La}_x\text{Co}_4\text{O}_9$  samples prepared in this work are very close to those found in the literature ( $\sim 0.24 \text{ nm}^3$ ) [32], for similar compositions. A minor variation of the unit cell size is also in accordance with that stated in Reference [35] for the  $\text{Ca}_{3-x}\text{Nd}_x\text{Co}_4\text{O}_9$  samples. However, in contrast, it has also been reported that the unit cell volume for some  $\text{Ca}_{2.7}\text{La}_{0.3}\text{Co}_4\text{O}_9$  samples (with higher nominal amounts of La) prepared via a nitrate self-combustion synthesis method increases slightly [34]. Still, the tendency observed in the present work is weak and comparable to the experimental error, being possibly affected by the formation of other phases, as discussed below.

General FESEM-EDS analyses revealed that all samples possess very similar grain morphology and microstructure (Figure 2). A relatively high degree of porosity, which is nonuniformly distributed in the bulk, is indicated by the black contrast. The porosity can be explained by the relatively low thermal and compositional stability of the  $\text{Ca}_3\text{Co}_4\text{O}_9$  phase (which is stable up to  $\sim 926 \text{ }^\circ\text{C}$  in air), when compared to the minimum temperature necessary to produce the liquid phase ( $\sim 1350 \text{ }^\circ\text{C}$ ) [41,42] to attain a good densification by conventional sintering. The highest degree of porosity can be seen for the  $\text{Ca}_{2.93}\text{La}_{0.07}\text{Co}_4\text{O}_9$  samples (Figure 2d). The complementary EDS analysis suggests that all  $\text{Ca}_{3-x}\text{La}_x\text{Co}_4\text{O}_9$  samples are mainly composed of the  $\text{Ca}_3\text{Co}_4\text{O}_9$  phase, with some small inclusions of the  $\text{Ca}_3\text{Co}_2\text{O}_6$  one, in agreement with the previously discussed XRD results. In Figure 2, both phases can be seen as having very similar contrasts and only present slightly different grain shapes and sizes, being hard to distinguish one phase from another with this technique. The major  $\text{Ca}_3\text{Co}_4\text{O}_9$  phase can be easily identified in Figure 2 as the plate-like grains with different orientation and of different shapes and sizes (a typical trait of the solid-state synthesis method). Lanthanum was detected by point EDS analyses in small ( $\sim 0.02 \text{ wt. } \%$ ) and large ( $\sim 0.1 \text{ wt. } \%$ ) amounts in  $\text{Ca}_{3-x}\text{La}_x\text{Co}_4\text{O}_9$  and  $\text{Ca}_{3-x}\text{La}_x\text{Co}_2\text{O}_6$ , respectively, similarly to the case of the substitution with Nd [35]. Some scattered white-contrast areas (in Figure 2c,d) correspond to La-rich phases, which appear at the highest substitution levels.

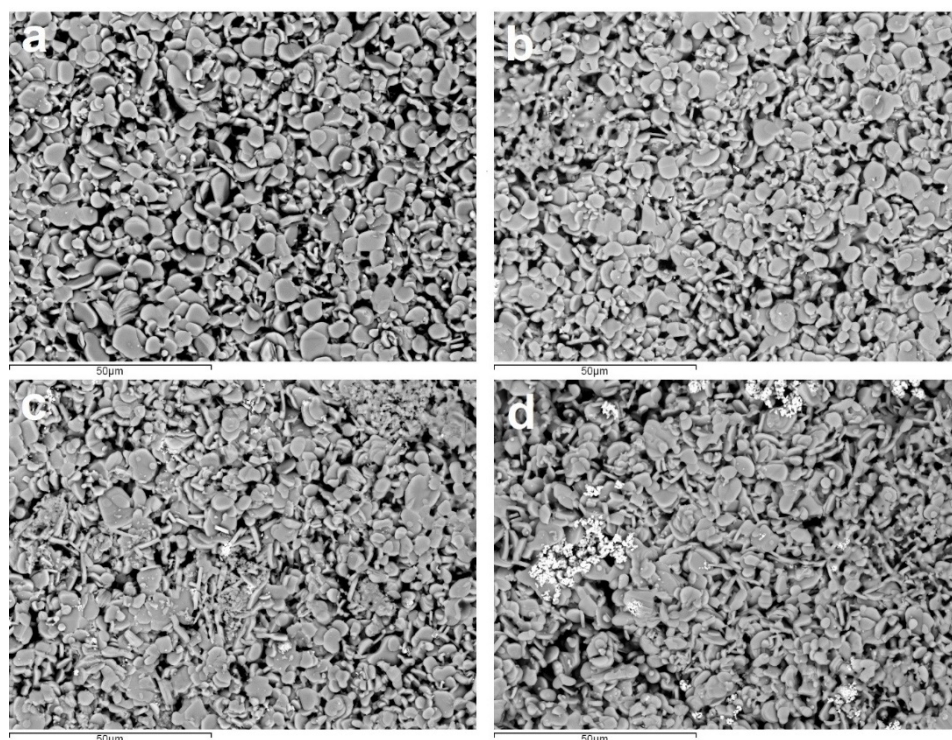


**Figure 2.** Representative FESEM micrographs (taken using back-scattered electrons) of selected longitudinal polished surface sections from  $\text{Ca}_{3-x}\text{La}_x\text{Co}_4\text{O}_9$  samples, with  $x = 0.01$  (a),  $0.03$  (b),  $0.05$  (c) and  $0.07$  (d).

More detailed point EDS analysis of the white-contrast areas from Figure 2c,d shows that they correspond to a  $(\text{La,Ca})\text{CoO}_3$  secondary phase, with a  $(\text{La} + \text{Ca}):\text{Co}$  ratio of 1:1. In the ternary equilibrium-phase diagram of the  $\text{CaO-La}_2\text{O}_3\text{-CoO}$  system [47], a  $\text{LaCoO}_3$  solid solution phase having a rhombohedral-distorted perovskite structure can be found. It can therefore be assumed that the secondary  $(\text{La,Ca})\text{CoO}_3$  phase identified by the EDS analysis corresponds to a  $\text{LaCoO}_3$ -based solid solution, which, however, was not detected by the XRD technique. The formation of these secondary phases can also be found in other experimental works from the literature [34] and are attributed to the higher stability of the perovskite-type  $\text{LaCoO}_3$  phase, as compared to  $\text{Ca}_{3-x}\text{La}_x\text{Co}_4\text{O}_9$  and  $\text{Ca}_{3-x}\text{La}_x\text{Co}_2\text{O}_6$ . For a closer view of the perovskite-type  $\text{LaCoO}_3$  phase, Figure 3 shows the morphology and microstructure of the additional secondary  $(\text{La} + \text{Ca})\text{CoO}_3$  phase in more detail for the  $\text{Ca}_{2.93}\text{La}_{0.07}\text{Co}_4\text{O}_9$  samples. These La-rich secondary phases discovered by the EDS analyses possess a very bright contrast and completely different morphology and microstructure, being easily distinguished as irregular grain shapes, with much smaller grain size ( $\leq 1.5 \mu\text{m}$ ). It should be noted that, in the case of Nd-substituted  $\text{Ca}_3\text{Co}_4\text{O}_9$  samples [35], the corresponding white-contrast inclusions were mainly attributed to the Nd-rich  $\text{Ca}_3\text{Co}_2\text{O}_6$  phase (for  $x \leq 0.05$ ). A different phase evolution for the  $\text{Ca}_{3-x}\text{La}_x\text{Co}_4\text{O}_9$  samples can be at least partially related to the higher thermodynamic stability of  $\text{LaCoO}_3$  as compared to  $\text{NdCoO}_3$  [48].

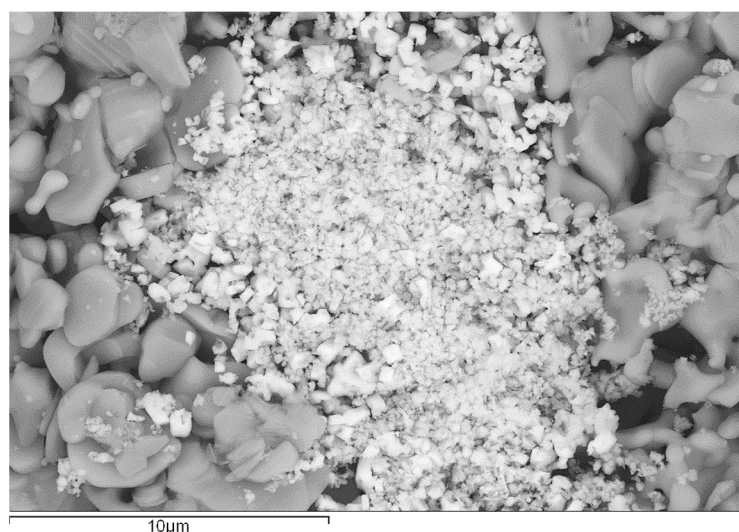


**Figure 3.** Representative high-magnification FESEM micrograph (taken using back-scattered electrons) of a selected longitudinal polished surface section of  $\text{Ca}_{2.93}\text{La}_{0.07}\text{Co}_4\text{O}_9$  sample, showing the lanthanum-rich phase.

The substitution with lanthanum does not seem to modify the morphology of the grains corresponding to the  $\text{Ca}_{3-x}\text{La}_x\text{Co}_4\text{O}_9$  or  $\text{Ca}_{3-x}\text{La}_x\text{Co}_2\text{O}_6$  phases, their mean sizes in all cases being estimated between 1 and 5  $\mu\text{m}$  in the planar dimension, equivalent to the  $a$ - $b$  crystallographic plane, and  $\sim 0.5 \mu\text{m}$  in thickness, along the direction of the  $c$ -axis, as in other, similar works found in the literature [49–51]. The approximate thickness of 0.5  $\mu\text{m}$  along the  $c$ -axis direction results from the pile up of very-thin plate-like grains of  $\text{Ca}_3\text{Co}_4\text{O}_9$ , each one measuring an individual thickness of  $\sim 35 \text{ nm}$  and exhibiting a preferential growth along the  $a$ - $b$  plane, as was estimated for similar polycrystalline layered cobaltites using Scherrer's formula [52].

The pristine and substituted samples show comparable apparent density values (Table 1) of  $\sim 72\%$  (for the  $x = 0.01, 0.03$  and  $0.05$  samples) of the theoretical value chosen for this work. The  $x = 0.07$  sample possesses a notably lower density (54% of the theoretical density). All other calculated densities are very close to other values found in the literature for similar compositions [35,50,51]. This indicates that the small substitutions with lanthanum do not improve the densification process during normal sintering. The relatively high porosity can be mostly attributed to the inefficient packing of the plate-like grains (low grain-packing density) during grain growth. The calculated density values support the previously discussed FESEM results, where the porosity was detected in all La-doped samples and especially in the  $\text{Ca}_{2.93}\text{La}_{0.07}\text{Co}_4\text{O}_9$  ones. The calculated decrease in density for the  $\text{Ca}_{2.95}\text{La}_{0.05}\text{Co}_4\text{O}_9$  and  $\text{Ca}_{2.93}\text{La}_{0.07}\text{Co}_4\text{O}_9$  samples can also be attributed to the formation of the secondary (La,Ca) $\text{CoO}_3$  phase (detected by the EDS analysis), which was most prevalent in the samples with the largest porosity ( $\text{Ca}_{2.93}\text{La}_{0.07}\text{Co}_4\text{O}_9$ ).

The variation of the Seebeck coefficient values with temperature for all  $\text{Ca}_{3-x}\text{La}_x\text{Co}_4\text{O}_9$  samples is shown in Figure 4. The sign of the thermopower is positive for all samples at all measured temperatures, confirming a conduction mechanism governed by  $p$ -type charge carriers, typical for the  $\text{Ca}_3\text{Co}_4\text{O}_9$  compound. The Seebeck coefficient values for all samples are very close and increase proportionally with temperature, following similar behavior and being almost independent of the La content. Similar trends were previously observed for Nd-substituted  $\text{Ca}_3\text{Co}_4\text{O}_9$  samples [35] for the same substitution levels.



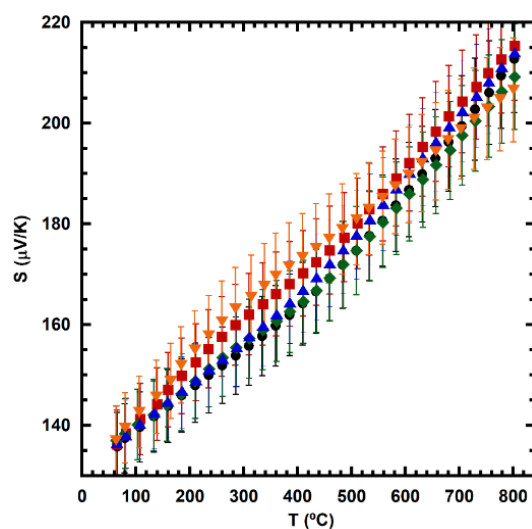


**Figure 4.** Temperature (T) dependence of the Seebeck coefficient (S) values for  $\text{Ca}_{3-x}\text{La}_x\text{Co}_4\text{O}_9$  samples, with  $x = 0.00$  (black circles), 0.01 (red squares), 0.03 (green diamonds), 0.05 (blue triangles) and 0.07 (orange inverse triangles).

These results indicate that the small substitutions with La performed in this study do not seem to significantly alter the charge carrier concentration from the conductive layers of the  $\text{Ca}_3\text{Co}_4\text{O}_9$  compound, which is to be expected, considering the higher oxidation state of the lanthanum ( $\text{La}^{3+}$ ) ions with respect to the calcium ( $\text{Ca}^{2+}$ ) ones. The comparable charge carrier concentrations in all samples were confirmed by the room-temperature cerimetric titrations, with which a mean cobalt valence of  $\sim 3.11$  was calculated in all cases. The highest S values measured at 800 °C ( $\sim 210 \mu\text{V/K}$ ) are, however, higher than some of the best-reported values in the literature, obtained for various high-density La-doped  $\text{Ca}_3\text{Co}_4\text{O}_9$  samples [33,53,54].

The electrical resistivity versus temperature graphs for the various  $\text{Ca}_{3-x}\text{La}_x\text{Co}_4\text{O}_9$  samples are shown in Figure 5. Between 50 and around 440 °C, all samples express a semiconducting-type behavior ( $d\rho/dT < 0$ ), followed by a metallic-type dependence ( $d\rho/dT > 0$ ) at higher temperatures. This transition temperature varies only slightly ( $\sim 20\text{--}40$  °C), for each composition. The  $\rho$  values measured for the  $x = 0.01, 0.03$  and 0.05 substituted samples are approximately the same, being lower than for the pristine composition. On the other hand, the  $\rho$  values of the  $\text{Ca}_{2.93}\text{La}_{0.07}\text{Co}_4\text{O}_9$  samples (around  $25 \text{ m}\Omega\cdot\text{cm}$ ) are notably higher than the reference in the entire measured temperature range. In these misfit layered cobaltites, a thermally activated hole-hopping (from  $\text{Co}^{4+}$  to  $\text{Co}^{3+}$ ) conduction mechanism is known to be behind the charge carrier transport from the semiconducting regime [55,56], while a more-simple valence or conduction band transport is attributed to the metallic conduction regime [35,57].

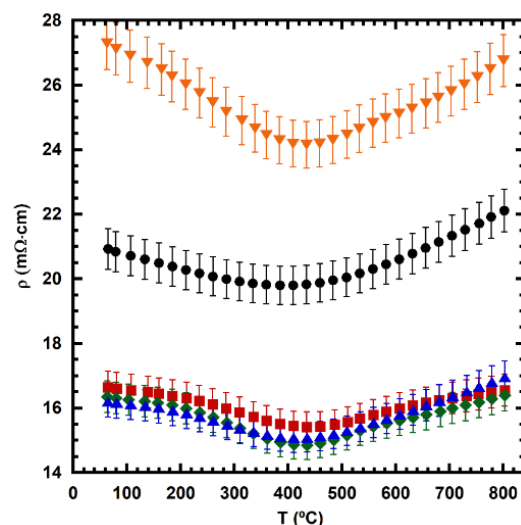


**Figure 5.** Temperature (T) dependence of the electrical resistivity ( $\rho$ ) values for  $\text{Ca}_{3-x}\text{La}_x\text{Co}_4\text{O}_9$  samples, with  $x = 0.00$  (black circles), 0.01 (red squares), 0.03 (green diamonds), 0.05 (blue triangles) and 0.07 (orange inverse triangles).

The electrical resistivity trends seen in Figure 5 can be easily explained on the basis of the highly anisotropic properties of the  $\text{Ca}_3\text{Co}_4\text{O}_9$  phase, which is widely known to present a metallic-like behavior in the direction of the  $a$ - $b$  plane and a semiconducting-like one in the direction of the  $c$ -axis [37]. Furthermore, when substituting  $\text{Ca}^{2+}$  with  $\text{La}^{3+}$  in the RS-type layers (which are regarded as an electrical charge reservoir for supplying charge carriers into the  $[\text{CoO}_2]$  layers), the resistivity values of all La-doped samples are expected to increase proportionally with lanthanum contents due to a consecutive, proportional decrease in the concentration of holes from the conductive layers along the  $a$ - $b$  planes. In particular, such a tendency was reported in Reference [32] for  $\text{Ca}_{3-x}\text{Ln}_x\text{Co}_4\text{O}_9$  ( $\text{Ln} = \text{La}, \text{Pr}, \text{Dy}$  and  $\text{Yb}$ ) samples when studying the compositions with  $x = 0, 0.1, 0.2, 0.3$ , the behavior being attributed to the simultaneous decrease in the charge carrier concentration and mobility. This does not seem to be the case in this study, where the electrical resistivity values measured for the samples with  $x = 0.01, 0.03$  and  $0.05$  (considered relatively similar, with a mean of around  $16 \text{ m}\Omega\cdot\text{cm}$ ) are around 1.3 times ( $21/16 \text{ m}\Omega\cdot\text{cm}$ ) or 24% ( $[(21 - 16)/21] \cdot 100$ ) lower than the  $\rho$  values measured for the pristine, reference sample (having a mean of around  $21 \text{ m}\Omega\cdot\text{cm}$ ). The latter indicates that the relevant effects may be different at relatively low substitution levels. Similar behavior was observed for low terbium contents in Tb-substituted  $\text{Ca}_3\text{Co}_4\text{O}_9$  samples [58]. In the case of  $\text{Ca}_{3-x}\text{Bi}_x\text{Co}_4\text{O}_9$  thin films, the resistivity was also found to decrease from  $x = 0$  to  $x = 0.4$  [59]. Finally, a significant decrease in resistivity was observed while incorporating a minor amount of Nd ( $x = 0.01$ ) into  $\text{Ca}_{3-x}\text{Nd}_x\text{Co}_4\text{O}_9$  samples [35]. This opposite effect can probably be explained by an increase in the charge carrier mobility, which, at low substitution levels, may dominate over the suppression of the charge carrier concentration. While comparing the relevant effects in  $\text{Ca}_{3-x}\text{La}_x\text{Co}_4\text{O}_9$  and  $\text{Ca}_{3-x}\text{Nd}_x\text{Co}_4\text{O}_9$  samples [35] for a similar substitution level, cation size effects could be considered. The ionic radius of six-fold coordinated  $\text{Ca}^{2+}$  ( $1.0 \text{ \AA}$ ) is slightly larger than for  $\text{Nd}^{3+}$  ( $0.983 \text{ \AA}$ ) and slightly smaller than for  $\text{La}^{3+}$  ( $1.032 \text{ \AA}$ ) [46]. This implies that opposite lattice stresses will be induced when Nd is replaced by La. Correspondingly, this might affect the charge compensation mechanism, facilitating the cobalt reduction and the corresponding increase in cobalt cation size in the case of smaller  $\text{Nd}^{3+}$ , with an opposite effect for larger  $\text{La}^{3+}$ . Interestingly, these assumptions correlate well with the resistivity behaviour seen in both systems: Further increase in Nd concentration to  $x = 0.03$  and  $x = 0.05$  impairs the charge carrier transport, presumably due to a decrease in the average oxidation state of cobalt and corresponding decrease in the charge carrier concentration, while  $\text{Ca}_{3-x}\text{La}_x\text{Co}_4\text{O}_9$  samples with  $x = 0.01, 0.03$  and  $0.05$  maintain similar

and notably lower resistivity as compared to the pristine, reference  $\text{Ca}_3\text{Co}_4\text{O}_9$  samples. Additional factors including local changes in the crystal structure and modifications of the misfit relationship between  $[\text{CoO}_2]$  and  $[\text{Ca}_2\text{CoO}_3]$  may also contribute to this complex behavior, as evidenced by Reference [60]. The highest resistivity values measured for the  $\text{Ca}_{2.93}\text{La}_{0.07}\text{Co}_4\text{O}_9$  samples (which also showed the lowest density value) can be attributed to a higher porosity and partial decomposition of the  $\text{Ca}_3\text{Co}_4\text{O}_9$  matrix, facilitated by the formation of the more stable  $(\text{La,Ca})\text{CoO}_3$  perovskite phase. In any case, the lowest resistivity values of the 0.01, 0.03 and 0.05 La-doped samples, measured at room temperature and 800 °C ( $\sim 16 \text{ m}\Omega\cdot\text{cm}$ ), are notably lower than some of the best values found in the literature ( $\sim 30 \text{ m}\Omega\cdot\text{cm}$  at room temperature and  $\sim 20 \text{ m}\Omega\cdot\text{cm}$  at around 730 °C) for  $\text{Ca}_{2.7}\text{La}_{0.3}\text{Co}_4\text{O}_9$  samples prepared by a conventional solid-state reaction method [32].

Finally, if the basic equation  $1/\rho = ne\mu$  [61] is applied using the module, with  $n$ ,  $e$  ( $=-1.602\cdot 10^{-19} \text{ C}$ ) and  $\mu$  ( $\approx 1 \text{ cm}^2\text{V}^{-1}\text{s}^{-1}$  [62]) standing for the concentration of holes, charge of the electron and the mobility of the holes, respectively, the concentration of holes  $n$  ( $=1/\rho e\mu$ ) comes out in the range  $37\text{--}42\cdot 10^{19} \text{ cm}^{-3}$  for the  $\text{Ca}_{3-x}\text{La}_x\text{Co}_4\text{O}_9$  samples with  $x = 0.01, 0.03$  and  $0.05$ , and in the range  $28\text{--}31\cdot 10^{19} \text{ cm}^{-3}$  for the reference  $\text{Ca}_3\text{Co}_4\text{O}_9$  samples. These values are slightly higher than the typical  $n$  values found in the literature ( $20\text{--}40\cdot 10^{19} \text{ cm}^{-3}$  [62]), for transition-metal-doped  $\text{Ca}_3\text{Co}_4\text{O}_9$  samples, and the  $n$  values for the  $\text{Ca}_{3-x}\text{La}_x\text{Co}_4\text{O}_9$  samples with  $x=0.01, 0.03$  and  $0.05$  are indeed slightly higher than those for the reference  $\text{Ca}_3\text{Co}_4\text{O}_9$  samples (in contrast with the  $n$  values for the low density  $\text{Ca}_{2.93}\text{La}_{0.07}\text{Co}_4\text{O}_9$  samples, which are found in the range  $23\text{--}26\cdot 10^{19} \text{ cm}^{-3}$ , being slightly lower than those for the reference), thus quantitatively explaining the minor effects of the small La substitutions on the charge carrier concentrations at higher temperatures.

The semiconducting-to-metallic transition temperature  $T^*$  can be clearly seen in Figure 6, where the modified Arrhenius plots for the various  $\text{Ca}_{3-x}\text{La}_x\text{Co}_4\text{O}_9$  samples are shown. The  $T^*$  values do not appear to vary significantly, in agreement with the previous resistivity results (a variation of  $\sim 20\text{--}40$  °C). The calculated activation energy (relative to the semiconducting regime) values  $E_a$  were found to be around 34 meV for the 0.03 and 0.05 La-doped samples,  $\sim 35$  meV for the 0.01 La-doped samples and  $\sim 37$  meV for the undoped, reference samples and 0.07 La-doped ones (also in Table 1), confirming that small substitutions of La do not have a great influence on the thermally activated hole-hopping process from the relevant temperature range, being partially responsible for the electrical conduction from these materials. The same trends can also be found elsewhere in the literature for similar cases and compositions [35,53,63–65].

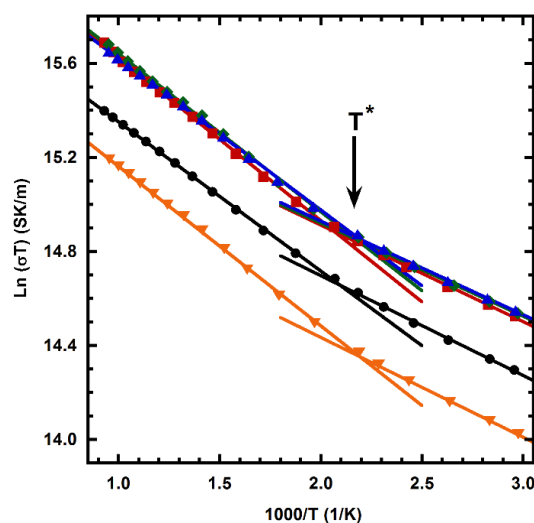


**Figure 6.** Modified  $\text{Ln}(\sigma T)$  versus  $1000/T$  Arrhenius plots for  $\text{Ca}_{3-x}\text{La}_x\text{Co}_4\text{O}_9$  samples, with  $x = 0.00$  (black circles),  $0.01$  (red squares),  $0.03$  (green diamonds),  $0.05$  (blue triangles) and  $0.07$  (orange inverse triangles).  $T^*$  indicates the semiconducting-to-metallic transition temperature.

The TE performance of the various  $\text{Ca}_{3-x}\text{La}_x\text{Co}_4\text{O}_9$  materials was finally evaluated using the PF values, plotted in Figure 7. The PF values of the samples with  $x = 0.01, 0.03$  and  $0.05$  are almost identical, while being higher than those measured for the reference, pristine composition. This improvement is mainly provided by the decrease in electrical resistivity, apparently stemming from the faster charge carrier transport outweighing the hole consumption effect on substitution with small amounts of La. The highest PF values, obtained for the  $0.01$  La-doped samples, are between  $\sim 22\%$  (at room temperature) and  $\sim 40\%$  (at  $800^\circ\text{C}$ ) higher than the ones obtained for the reference, non-substituted samples.

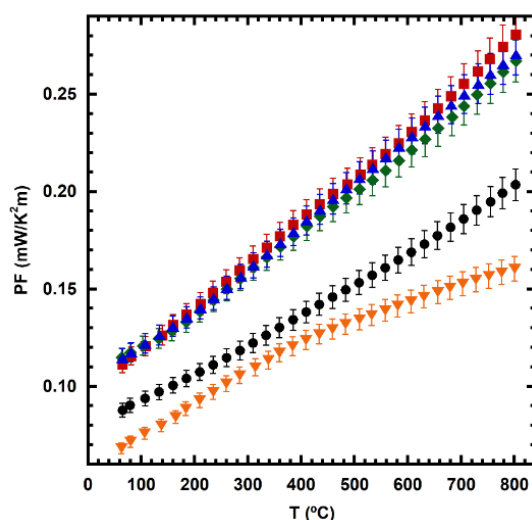


**Figure 7.** Temperature ( $T$ ) dependence of the power factor (PF) values for  $\text{Ca}_{3-x}\text{La}_x\text{Co}_4\text{O}_9$  samples, with  $x = 0.00$  (black circles),  $0.01$  (red squares),  $0.03$  (green diamonds),  $0.05$  (blue triangles) and  $0.07$  (orange inverse triangles).



#### 4. Conclusions

In this study,  $\text{Ca}_{3-x}\text{La}_x\text{Co}_4\text{O}_9$  samples with  $x = 0.00, 0.01, 0.03, 0.05$  and  $0.07$  were successfully synthesized and processed through a classical solid-state route, chosen for its simplicity, and their high-temperature electrical properties were analyzed and related to their composition, morphology and microstructural features.

- The  $\text{La}^{3+}$  ions were found to substitute the  $\text{Ca}^{2+}$  ones in the  $\text{Ca}_3\text{Co}_4\text{O}_9$  phase, only in small amounts ( $x < 0.03$ ), disturbing the electron–hole symmetry from the conductive  $\text{CoO}_2$  layers and improving the mobile hole conduction in the corresponding samples.
- The microstructural characterizations showed that the ceramic morphology is mostly unaffected by the substitutions with lanthanum, except for the  $\text{Ca}_{2.93}\text{La}_{0.07}\text{Co}_4\text{O}_9$  samples, which showed an additional secondary phase with very distinct morphology of its grains.
- Higher levels of La substitutions ( $x > 0.03$ ) were found to promote the secondary  $\text{Ca}_3\text{Co}_2\text{O}_6$  phase formation and, further on, of the  $(\text{La,Ca})\text{CoO}_3$  phase in the  $\text{Ca}_{2.93}\text{La}_{0.07}\text{Co}_4\text{O}_9$  samples with the largest substitutions from this work.
- The PF values calculated for the  $0.01, 0.03$  and  $0.05$  La-doped samples are almost identical and higher than for the pristine  $\text{Ca}_3\text{Co}_4\text{O}_9$  samples, provided by their lower electrical resistivity and caused by a possible increase in charge carrier concentration and/or mobility.
- Higher substitution levels ( $x > 0.05$ ) resulted in the appearance of additional porosity and a noticeable decrease in electrical performance in the  $\text{Ca}_{2.93}\text{La}_{0.07}\text{Co}_4\text{O}_9$  samples.
- The highest PF values at  $50$  and  $800^\circ\text{C}$ , calculated for the  $0.01$  La-doped samples ( $\sim 0.11$  and  $\sim 0.28$   $\text{mW/K}^2\text{m}$  respectively), are around  $31\%$  higher than for the pristine  $\text{Ca}_3\text{Co}_4\text{O}_9$  materials used as reference.

These conclusions suggest that small substitutions with rare-earth metals in the RS-type layers are a promising pathway for boosting the high-temperature electrical performance of the strongly correlated  $\text{Ca}_3\text{Co}_4\text{O}_9$  compound, known to be highly susceptible to even the slightest breaks in the electron–hole symmetry of the conductive layers of its structure.

**Author Contributions:** Conceptualization, G.C., A.V.K., J.C.D. and A.S.; Data curation, G.C., S.R. and D.V.L.; Formal analysis, G.C., S.R., A.V.K., J.C.D., A.S., M.A.M. and M.A.T.; Funding acquisition, G.C. and A.V.K.; Investigation, G.C., S.R., P.A., D.V.L., M.A.V., M.A.M. and M.A.T.; Methodology, G.C., S.R., D.V.L., A.V.K., A.S. and M.A.M.; Project administration, G.C. and A.V.K.; Software, G.C. and S.R.; Supervision, A.V.K., J.C.D. and A.S.; Validation, G.C., S.R., P.A., D.V.L. and M.A.V.; Visualization, G.C., S.R., P.A., D.V.L., M.A.V. and A.V.K.; Writing—original draft, G.C., A.V.K. and A.S.; Writing—review and editing, G.C., S.R., P.A., D.V.L., M.A.V., A.V.K., J.C.D., M.A.M. and M.A.T. All authors have read and agreed to the published version of the manuscript.

**Funding:**  This project has received funding from the European Union’s Horizon 2020 research and innovation programme .

**Institutional Review Board Statement:** Not applicable.

**Data Availability Statement:** Data sharing not available.

**Acknowledgments:** G. Constantinescu acknowledges the support of the TEOsINTE project (Grant agreement ID: 101003375), funded under the H2020-EU.4. Programmes (Funding Scheme: MSCA-IF-EF-ST—Standard EF). Partial support of the project REMOTE (POCI-01-0145-FEDER-031875) is also acknowledged. This work was partially developed within the scope of the project CICECO-Aveiro Institute of Materials, UIDB/50011/2020 and UIDP/50011/2020, financed by national funds through the Portuguese Foundation for Science and Technology/MCTES. J.C. Diez, A. Sotelo, M.A. Madre and M.A. Torres acknowledge the financial support of the Spanish MINECO-FEDER project MAT2017-82183-C3-1-R and the Aragón Government (Research Group T54-20R). The technical contributions of C. Estepa, and C. Gallego are highly appreciated and acknowledged. Sh. Rasekh acknowledges the support of the Research Employment Contract FCT–CEECIND/02608/2017. P. Amirkhizi acknowledges the financial support of the Portuguese FCT Doctoral Studentship 2020.08051.BD. D. V. Lopes acknowledges the financial support of the research fellowship BI/UI50/9051/2020 provided by the European Commission (project SIDERWIN-DLV-768788—Horizon 2020/SPIRE10).

**Conflicts of Interest:** The authors declare no conflict of interest. The funders had no role in the design of the study; in the collection, analyses, or interpretation of data; in the writing of the manuscript or in the decision to publish the results.

## References

1. Rowe, D.M. *Thermoelectrics Handbook: Macro to Nano*, 1st ed.; CRC Press: Boca Raton, FL, USA, 2006; pp. 1–3–1–7.
2. Freer, R.; Powell, A.V. Realising the potential of thermoelectric technology: A Roadmap. *J. Mater. Chem. C* **2020**, *8*, 441–463.
3. Bahrami, A.; Schierning, G.; Nielsch, K. Waste Recycling in Thermoelectric Materials. *Adv. Energy Mater.* **2020**, *10*, doi:10.1002/aenm.201904159.
4. Beretta, D.; Neophytou, N.; Hodges, J.M.; Kanatzidis, M.G.; Narducci, D.; Martin-Gonzalez, M.; Beekman, M.; Balke, B.; Cerretti, G.; Tremel, W.; et al. Thermoelectrics: From history, a window to the future. *Mater. Sci. Eng. R Rep.* **2019**, *138*, 100501, doi:10.1016/j.mser.2018.09.001.
5. Mahan, G.; Sales, B.; Sharp, J. Thermoelectric materials: New approaches to an old problem. *Phys. Today* **1997**, *50*, 42–47, doi:10.1063/1.881752.
6. Naito, H.; Kohsaka, Y.; Cooke, D.; Arashi, H. Development of a solar receiver for a high-efficiency thermionic/thermoelectric conversion system. *Sol. Energy* **1996**, *58*, 191–195.
7. Kim, C.M.; Hwang, Y.J.; Ryu, Y.H. Air Conditioner for Individual Cooling/Heating. US Patent US6393842, 28 May 2002.
8. Liu, W.; Lukas, K.C.; McEnaney, K.; Lee, S.; Zhang, Q.; Opeil, C.P.; Chen, G.; Ren, Z. Studies on the  $\text{Bi}_2\text{Te}_3\text{-Bi}_2\text{Se}_3\text{-Bi}_2\text{S}_3$  system for mid-temperature thermoelectric energy conversion. *Energy Environ. Sci.* **2013**, *6*, 552–560, doi:10.1039/c2ee23549h.
9. Artini, C.; Carlini, R.; Spotorno, R.; Failamani, F.; Mori, T.; Mele, P. Structural properties and thermoelectric performance of the double-filled skutterudite  $(\text{Sm,Gd})_y(\text{Fe,Ni}_{1-x})_4\text{Sb}_{12}$ . *Materials* **2019**, *12*, 2451, doi:10.3390/ma12152451.
10. Terasaki, I.; Sasago, Y.; Uchinokura, K. Large thermoelectric power in single crystals. *Phys. Rev. B Condens. Matter Mater. Phys.* **1997**, *56*, R12685–R12687, doi:10.1103/PhysRevB.56.R12685.

11. Sotelo, A.; Rasekh, S.; Madre, M.A.; Guilmeau, E.; Marinel, S.; Diez, J.C. Solution-based synthesis routes to thermoelectric Bi<sub>2</sub>Ca<sub>2</sub>Co<sub>1.7</sub>O<sub>x</sub>. *J. Eur. Ceram. Soc.* **2011**, *31*, 1763–1769, doi:10.1016/j.jeurceramsoc.2011.03.008.
12. Madre, M.A.; Rasekh, S.; Diez, J.C.; Sotelo, A. New solution method to produce high performance thermoelectric ceramics: A case study of Bi-Sr-Co-O. *Mater. Lett.* **2010**, *64*, 2566–2568, doi:10.1016/j.matlet.2010.08.041.
13. Constantinescu, G.; Rasekh, S.; Torres, M.A.; Madre, M.A.; Diez, J.C.; Sotelo, A. Enhancement of the high-temperature thermoelectric performance of Bi<sub>2</sub>Ba<sub>2</sub>Co<sub>2</sub>O<sub>x</sub> ceramics. *Scr. Mater.* **2013**, *68*, 75–78, doi:10.1016/j.scriptamat.2012.09.014.
14. Funahashi, R.; Matsubara, I.; Ikuta, H.; Takeuchi, T.; Mizutani, U.; Sodeoka, S. Oxide single crystal with high thermoelectric performance in air. *Jpn. J. Appl. Phys.* **2000**, *39*, L1127, doi:10.1143/jjap.39.L1127.
15. Torres, M.A.; Costa, F.M.; Flahaut, D.; Touati, K.; Rasekh, S.; Ferreira, N.M.; Allouche, J.; Depriester, M.; Madre, M.A.; Kovalevsky, A.V.; et al. Significant enhancement of the thermoelectric performance in Ca<sub>3</sub>Co<sub>4</sub>O<sub>9</sub> thermoelectric materials through combined strontium substitution and hot-pressing process. *J. Eur. Ceram. Soc.* **2019**, *39*, 1186–1192, doi:10.1016/j.jeurceramsoc.2018.12.049.
16. Maignan, A.; Pelloquin, D.; Hebert, S.; Klein, Y.; Hervieu, M. Thermoelectric power in misfit cobaltites ceramics: Optimization by chemical substitutions. *Bol. Soc. Esp. Ceram. Vidr.* **2006**, *45*, 122–125.
17. Maignan, A.; Hébert, S.; Hervieu, M.; Michel, C.; Pelloquin, D.; Khomskii, D. Magnetoresistance and Magnetothermopower Properties of Bi/Ca/Co/O and Bi(Pb)/Ca/Co/O Misfit Layer Cobaltites. Available online: <https://iopscience.iop.org/article/10.1088/0953-8984/15/17/323> (accessed on 17 July 2020).
18. Yang, G.; Ramasse, Q.; Klie, R.F. Direct measurement of charge transfer in thermoelectric Ca<sub>3</sub>Co<sub>4</sub>O<sub>9</sub>. *Phys. Rev. B Condens. Matter Mater. Phys.* **2008**, *78*, 153109, doi:10.1103/PhysRevB.78.153109.
19. Demirel, S.; Aksan, M.A.; Altin, S. Low temperature electrical and thermal transport properties of the Ca<sub>3-x</sub>Sb<sub>x</sub>Co<sub>4</sub>O<sub>9</sub> system. *J. Mater. Sci. Mater. Electron.* **2012**, *23*, 2251–2256, doi:10.1007/s10854-012-0792-8.
20. Sotelo, A.; Rasekh, S.; Guilmeau, E.; Madre, M.A.; Torres, M.A.; Marinel, S.; Diez, J.C. Improved thermoelectric properties in directionally grown Bi<sub>2</sub>Sr<sub>2</sub>Co<sub>1.8</sub>O<sub>y</sub> ceramics by Pb for Bi substitution. *Mater. Res. Bull.* **2011**, *46*, 2537–2542, doi:10.1016/j.materresbull.2011.08.011.
21. Sotelo, A.; Guilmeau, E.; Rasekh, S.H.; Madre, M.A.; Marinel, S.; Diez, J.C. Enhancement of the thermoelectric properties of directionally grown Bi-Ca-Co-O through Pb for Bi substitution. *J. Eur. Ceram. Soc.* **2010**, *30*, 1815–1820, doi:10.1016/j.jeurceramsoc.2010.01.037.
22. Mikami, M.; Ando, N.; Funahashi, R. The effect of Ag addition on electrical properties of the thermoelectric compound Ca<sub>3</sub>Co<sub>4</sub>O<sub>9</sub>. *J. Solid State Chem.* **2005**, *178*, 2186–2190, doi:10.1016/j.jssc.2005.04.027.
23. Kahraman, F.; Madre, M.A.; Rasekh, S.; Salvador, C.; Bosque, P.; Torres, M.A.; Diez, J.C.; Sotelo, A. Enhancement of mechanical and thermoelectric properties of Ca<sub>3</sub>Co<sub>4</sub>O<sub>9</sub> by Ag addition. *J. Eur. Ceram. Soc.* **2015**, *35*, 3835–3841, doi:10.1016/j.jeurceramsoc.2015.05.029.
24. Sotelo, A.; Torres, M.A.; Constantinescu, G.; Rasekh, S.; Diez, J.C.; Madre, M.A. Effect of Ag addition on the mechanical and thermoelectric performances of annealed Bi<sub>2</sub>Sr<sub>2</sub>Co<sub>1.8</sub>O<sub>x</sub> textured ceramics. *J. Eur. Ceram. Soc.* **2012**, *32*, 3745–3751, doi:10.1016/j.jeurceramsoc.2012.05.035.
25. Sotelo, A.; Rasekh, S.; Constantinescu, G.; Torres, M.A.; Madre, M.A.; Diez, J.C. Improvement of textured Bi<sub>1.6</sub>Pb<sub>0.4</sub>Sr<sub>2</sub>Co<sub>1.8</sub>O<sub>x</sub> thermoelectric performances by metallic Ag additions. *Ceram. Int.* **2013**, *39*, 1597–1602, doi:10.1016/j.ceramint.2012.07.112.
26. Madre, M.A.; Urrutibeascoa, I.; García, G.; Torres, M.A.; Sotelo, A.; Diez, J.C. High-Temperature Stability of Hot-Pressed Sr-Doped Ca<sub>3</sub>Co<sub>4</sub>O<sub>9</sub>. *J. Electron. Mater.* **2019**, *48*, 1965–1970, doi:10.1007/s11664-018-6748-x.
27. Noudem, J.G.; Kenfaui, D.; Chateigner, D.; Gomina, M. Toward the enhancement of thermoelectric properties of lamellar Ca<sub>3</sub>Co<sub>4</sub>O<sub>9</sub> by edge-free spark plasma texturing. *Scr. Mater.* **2012**, *66*, 258–260, doi:10.1016/j.scriptamat.2011.11.004.
28. Miyazawa, K.; Amaral, F.; Kovalevsky, A.V.; Graça, M.P.F. Hybrid microwave processing of Ca<sub>3</sub>Co<sub>4</sub>O<sub>9</sub> thermoelectrics. *Ceram. Int.* **2016**, *42*, 9482–9487, doi:10.1016/j.ceramint.2016.03.015.
29. Ferreira, N.M.; Rasekh, S.; Costa, F.M.; Madre, M.A.; Sotelo, A.; Diez, J.C.; Torres, M.A. New method to improve the grain alignment and performance of thermoelectric ceramics. *Mater. Lett.* **2012**, *83*, 144–147, doi:10.1016/j.matlet.2012.05.131.
30. Diez, J.C.; Rasekh, S.; Constantinescu, G.; Costa, F.M.; Ferreira, N.M.; Torres, M.A.; Madre, M.A.; Sotelo, A. High Thermoelectric Performances in Co-oxides Processed by a Laser Floating Zone Technique. *Mater. Today Proc.* **2015**, *2*, 654–660, doi:10.1016/j.matpr.2015.05.091.
31. Tani, T.; Itahara, H.; Kadoura, H.; Asahi, R. Crystallographic orientation analysis on calcium cobaltite ceramic grains textured by reactive-templated grain growth. *Int. J. Appl. Ceram. Technol.* **2007**, *4*, 318–325, doi:10.1111/j.1744-7402.2007.02146.x.
32. Wang, Y.; Sui, Y.; Li, F.; Xu, L.; Wang, X.; Su, W.; Liu, X. Thermoelectrics in misfit-layered oxides [(Ca,Ln)<sub>2</sub>CoO<sub>3</sub>]<sub>0.62</sub>[CoO<sub>2</sub>]<sub>2</sub>: From bulk to nano. *Nano Energy* **2012**, *1*, 456–465, doi:10.1016/j.nanoen.2012.02.007.
33. Liu, Y.; Zhang, L.; Shirsath, S.E.; Zheng, J.; Liu, Y.; Ulrich, C.; Li, S. Manipulation of charge carrier concentration and phonon scattering via spin-entropy and size effects: Investigation of thermoelectric transport properties in La-doped Ca<sub>3</sub>Co<sub>4</sub>O<sub>9</sub>. *J. Alloys Compd.* **2019**, *801*, 60–69, doi:10.1016/j.jallcom.2019.06.113.
34. Ben Yahia, H.; Mauvy, F.; Grenier, J.C. Ca<sub>3-x</sub>LaxCo<sub>4</sub>O<sub>9+δ</sub> (x = 0, 0.3): New cobaltite materials as cathodes for proton conducting solid oxide fuel cell. *J. Solid State Chem.* **2010**, *183*, 527–531, doi:10.1016/j.jssc.2009.12.014.
35. Constantinescu, G.; Torres, M.A.; Rasekh, S.; Madre, M.A.; Diez, J.C.; Sotelo, A. Modification of thermoelectric properties in Ca<sub>3</sub>Co<sub>4</sub>O<sub>y</sub> ceramics by Nd doping. *J. Mater. Sci. Mater. Electron.* **2014**, *25*, 922–927, doi:10.1007/s10854-013-1665-5.

36. Rodríguez-Carvajal, J. Recent advances in magnetic structure determination by neutron powder diffraction. *Phys. B Phys. Condens. Matter* **1993**, *192*, 55–69, doi:10.1016/0921-4526(93)90108-I.
37. Masset, A.; Michel, C.; Maignan, A.; Hervieu, M.; Toulemonde, O.; Studer, F.; Raveau, B.; Hejtmanek, J. Misfit-layered cobaltite with an anisotropic giant magnetoresistance. *Phys. Rev. B Condens. Matter Mater. Phys.* **2000**, *62*, 166–175, doi:10.1103/PhysRevB.62.166.
38. Madre, M.A.; Costa, F.M.; Ferreira, N.M.; Sotelo, A.; Torres, M.A.; Constantinescu, G.; Rasekh, S.; Diez, J.C. Preparation of high-performance Ca<sub>3</sub>Co<sub>4</sub>O<sub>9</sub> thermoelectric ceramics produced by a new two-step method. *J. Eur. Ceram. Soc.* **2013**, *33*, 1747–1754, doi:10.1016/j.jeurceramsoc.2013.01.029.
39. Roisnel, T.; Rodríguez-Carvajal, J. WinPLOTR: A Windows tool for powder diffraction patterns analysis Materials Science Forum, Proceedings of the Seventh European Powder Diffraction Conference (EPDIC 7). R. Delhez E J. Mittenmeijer **2000**, 118–123.
40. Brisi, C.; Rolando, P. Ricerche sul sistema ossido di calcio-ossido cobaltoso-ossigeno. *Ann. Chim.* **1968**, *58*, 676–683.
41. Woermann, E.; Muan, A. Phase equilibria in the system CaO-cobalt oxide in air. *J. Inorg. Nucl. Chem.* **1970**, *32*, 1455–1459, doi:10.1016/0022-1902(70)80631-5.
42. Sedmidubský, D.; Jakeš, V.; Jankovský, O.; Leitner, J.; Sofer, Z.; Hejtmánek, J. Phase equilibria in Ca-Co-O system. *J. Solid State Chem.* **2012**, *194*, 199–205, doi:10.1016/j.jssc.2012.05.014.
43. Fjellvåg, H.; Gulbrandsen, E.; Aasland, S.; Olsen, A.; Hauback, B.C. Crystal Structure and Possible Charge Ordering in One-Dimensional Ca<sub>3</sub>Co<sub>2</sub>O<sub>6</sub>. *J. Solid State Chem.* **1996**, *124*, 190–194.
44. Takahashi, J.; Yamane, H.; Shimada, M. Thermoelectric Properties of Ca<sub>3</sub>Co<sub>2</sub>O<sub>6</sub> Single Crystal. *Jpn. J. Appl. Phys.* **2004**, *43*, L331–L333.
45. Bezdicka, P. Academy of Sciences of the Czech Republic, Inst. of Inorganic Chemistry, Rezu Praha, Czech Republic. ICDD Grant-in-Aid 1999. Available online: <https://www.icdd.com/> (accessed on 13 May 2019).
46. Shannon, R.D. Revised effective ionic radii and systematic studies of interatomic distances in halides and chalcogenides. *Acta Crystallogr. Sect. A* **1976**, *32*, 751–767, doi:10.1107/S0567739476001551.
47. Cherepanov, V.A.; Gavrilova, L.Y.; Barkhatova, L.Y.; Voronin, V.I.; Trifonova, M.V.; Bukhner, O.A. Phase Equilibria in the La-Me-Co-O (Me = Ca, Sr, Ba) Systems. *Ionics* **1998**, *4*, 309.
48. Sahu, S.K.; Tanasescu, S.; Scherrer, B.; Marinescu, C.; Navrotsky, A. Energetics of lanthanide cobalt perovskites: LnCoO<sub>3-δ</sub> (Ln = La, Nd, Sm, Gd). *J. Mater. Chem. A* **2015**, *3*, 19490–19496, doi:10.1039/c5ta03655k.
49. Matsubara, I.; Funahashi, R.; Takeuchi, T.; Sodeoka, S. *Thermoelectric Properties of Spark Plasma Sintered Ca<sub>2.75</sub>Gd<sub>0.25</sub>Co<sub>4</sub>O<sub>9</sub> ceramics*; American Institute of Physics AIP: College Park, MD, USA, 2001; Volume 90, pp. 462–465.
50. Song, X.; Chen, Y.; Chen, S.; Barbero, E.; Thomas, E.L.; Barnes, P. Significant enhancement of electrical transport properties of the thermoelectric Ca<sub>3</sub>Co<sub>4</sub>O<sub>9-δ</sub> through Yb doping. *Solid State Commun.* **2012**, *152*, 1509–1512, doi:10.1016/j.ssc.2012.06.014.
51. Rasekh, S.; Constantinescu, G.; Torres, M.A.; Diez, J.C.; Madre, M.A.; Sotelo, A. Thermoelectric properties of rare earth doped Ca<sub>3-x</sub>RE<sub>x</sub>Co<sub>4</sub>O<sub>9</sub> (RE = Dy, Er, Gd, and Tb; X = 0, 0.01, 0.03, and 0.05). *J. Electroceram.* **2014**, *32*, 376–382, doi:10.1007/s10832-014-9925-1.
52. Torres, M.A.; Sotelo, A.; Rasekh, S.; Serrano, I.; Constantinescu, G.; Madre, M.A.; Diez, J.C. Improvement of thermoelectric properties of Bi<sub>2</sub>Sr<sub>2</sub>Co<sub>1.8</sub>O<sub>x</sub> through solution synthetic methods. *Bol. Soc. Esp. Ceram. Vidr.* **2012**, *51*, 1–6, doi:10.3989/cyv.012012.
53. Song, Y.; Nan, C.W. High temperature transport properties of Ag-added (Ca<sub>0.975</sub>La<sub>0.025</sub>)<sub>3</sub>Co<sub>4</sub>O<sub>9</sub> ceramics. *Phys. B Condens. Matter* **2011**, *406*, 2919–2923, doi:10.1016/j.physb.2011.05.006.
54. Lin, Y.H.; Nan, C.W.; Liu, Y.; Li, J.; Mizokawa, T.; Shen, Z. High-temperature electrical transport and thermoelectric power of partially substituted Ca<sub>3</sub>Co<sub>4</sub>O<sub>9</sub>-based ceramics. *J. Am. Ceram. Soc.* **2007**, *90*, 132–136, doi:10.1111/j.1551-2916.2006.01370.x.
55. Lin, Y.H.; Lan, J.; Shen, Z.; Liu, Y.; Nan, C.W.; Li, J.F. High-temperature electrical transport behaviors in textured Ca<sub>3</sub>Co<sub>4</sub>O<sub>9</sub>-based polycrystalline ceramics. *Appl. Phys. Lett.* **2009**, *94*, doi:10.1063/1.3086875.
56. Mott, N.F.; Jones, H. *The Theory of the Properties of Metals and Alloys*; Dover: New York, NY, USA, 1958; p. 305.
57. Pinitsoontorn, S.; Lersongkram, N.; Keawprak, N.; Amornkitbamrung, V. Thermoelectric properties of transition metals-doped Ca<sub>3</sub>Co<sub>3.8</sub>M<sub>0.2</sub>O<sub>9δ</sub> (M = Co, Cr, Fe, Ni, Cu and Zn). *J. Mater. Sci. Mater. Electron.* **2012**, *23*, 1050–1056, doi:10.1007/s10854-011-0546-z.
58. Saini, S.; Yaddanapudi, H.S.; Tian, K.; Yin, Y.; Maggini, D.; Tiwari, A. Terbium Ion Doping in Ca<sub>3</sub>Co<sub>4</sub>O<sub>9</sub>: A Step towards High-Performance Thermoelectric Materials. *Sci. Rep.* **2017**, *7*, srep44621, doi:10.1038/srep44621.
59. Sun, T.; Hng, H.H.; Yan, Q.Y.; Ma, J. Enhanced high temperature thermoelectric properties of Bi-doped c-axis oriented Ca<sub>3</sub>Co<sub>4</sub>O<sub>9</sub> thin films by pulsed laser deposition. *J. Appl. Phys.* **2010**, *108*, 83709, doi:10.1063/1.3499324.
60. Mikami, M.; Chong, K.; Miyazaki, Y.; Kajitani, T.; Inoue, T.; Sodeoka, S.; Funahashi, R. Bi-substitution effects on crystal structure and thermoelectric properties of Ca<sub>3</sub>Co<sub>4</sub>O<sub>9</sub> single crystals. *Jpn. J. Appl. Phys. Part 1 Regul. Pap. Short Notes Rev. Pap.* **2006**, *45*, 4131–4136, doi:10.1143/JJAP.45.4131.
61. Snyder, G.J.; Toberer, E.S. Complex thermoelectric materials. *Nat. Mater.* **2008**, *7*, 105–114, doi:10.1038/nmat2090.
62. Wang, Y.; Sui, Y.; Wang, X.; Su, W.; Liu, X. Enhanced high temperature thermoelectric characteristics of transition metals doped Ca<sub>3</sub>Co<sub>4</sub>O<sub>9+δ</sub> by cold high-pressure fabrication. *J. Appl. Phys.* **2010**, *107*, 033708, doi:10.1063/1.3291125.
63. Wang, D.; Chen, L.; Wang, Q.; Li, J. Fabrication and thermoelectric properties of Ca<sub>3-x</sub>Dy<sub>x</sub>Co<sub>4</sub>O<sub>9+δ</sub> system. *J. Alloys Compd.* **2004**, *376*, 58–61, doi:10.1016/j.jallcom.2003.12.018.

- 
64. Bhaskar, A.; Jhang, C.S.; Liu, C.J. Thermoelectric properties of  $\text{Ca}_{3-x}\text{Dy}_x\text{Co}_4\text{O}_{9+\delta}$  with  $x=0.00, 0.02, 0.05,$  and  $0.10$ . *J. Electron. Mater.* **2013**, *42*, 2582–2586, doi:10.1007/s11664-013-2634-8.
  65. Pei, J.; Chen, G.; Lu, D.Q.; Liu, P.S.; Zhou, N. *Synthesis and High Temperature Thermoelectric Properties of  $\text{Ca}_{3.0-x-y}\text{Nd}_x\text{NayCo}_4\text{O}_{9+\delta}$* ; Pergamon: Oxford, UK, 2008; Volume 146, pp. 283–286.